The Astrophysical Journal, 884:132 (14pp), 2019 October 20 https://doi.org/10.3847/1538-4357/ab4260

Stable Radio Core of the Blazar Mrk 501 during High-energy Active State in 2012

Shoko Koyama[1], Motoki Kino[2,3], Akihiro Doi[4], Kotaro Niinuma[5], Marcello Giroletti[6], David Paneque[7], Kazunori Akiyama[3,8,9,10], Gabriele Giovannini[6,11], Guang-Yao Zhao[12], Eduardo Ros[13], Jun Kataoka[14], Monica Orienti[6], Kazuhiro Hada[3], Hiroshi Nagai[3], Naoki Isobe[4], Hideyuki Kobayashi[3,15], Mareki Honma[3,15], and Rocco Lico[13]

[1] Institute of Astronomy & Astrophysics, Academia Sinica, P.O. Box 23-141, Taipei 10617, Taiwan; skoyama@asiaa.sinica.edu.tw
[2] Kogakuin University, Academic Support Center, 2665-1 Nakano, Hachioji, Tokyo 192-0015, Japan
[3] National Astronomical Observatory of Japan, 2-21-1 Osawa, Mitaka, Tokyo, 181-8588, Japan
[4] Institute of Space and Astronautical Science (ISAS), Japan Aerospace Exploration Agency (JAXA), 3-1-1 Yoshinodai, Chuo-ku, Sagamihara, Kanagawa 252-5210, Japan
[5] Graduate School of Science and Engineering, Yamaguchi University, Yoshida 1677-1, Yamaguchi, Yamaguchi 753-8512, Japan
[6] INAF Istituto di Radioastronomia, via Gobetti 101, I-40129 Bologna, Italy
[7] Max-Planck-Institut für Physik, D-80805 München, Germany
[8] National Radio Astronomy Observatory, 520 Edgemont Rd., Charlottesville, VA 22903, USA
[9] Massachusetts Institute of Technology, Haystack Observatory, 99 Millstone Rd., Westford, MA 01886, USA
[10] Black Hole Initiative, Harvard University, 20 Garden Street, Cambridge, MA 02138, USA
[11] Dipartimento di Astronomia, Università di Bologna, via Ranzani 1, I-40127 Bologna, Italy
[12] Korea Astronomy and Space Science Institute, Daedeokdae-ro 776, Yuseong-gu, Daejeon 305-348, Republic of Korea
[13] Max-Planck-Institut für Radioastronomie, Auf dem Hügel 69, D-53121 Bonn, Germany
[14] Research Institute for Science and Engineering, Waseda University, 3-4-1, Okubo, Shinjuku, Tokyo 169-8555, Japan
[15] Department of Astronomy, School of Physical Sciences, The Graduate University for Advanced Studies, SOKENDAI, 2-21-1 Osawa, Mitaka, Tokyo 181-8588, Japan

Received 2019 January 7; revised 2019 August 9; accepted 2019 September 5; published 2019 October 18

Abstract

We investigate the precise location of the radio core in the nearby blazar Mrk 501 for the first time during its X-ray and TeV γ-ray active state in 2012 by revisiting from the perspective of astrometry the six-epoch observations with the Very Long Baseline Array at 43 GHz reported by Koyama et al. We find that the position of the radio core seen at 43 GHz remained stable during our observations from 2012 to 2013 February within 42 μas in the southeast jet direction and 56 μas along the northeast jet direction. This implies that the location of the 43 GHz radio-emitting core was limited within the deprojected scale of 4.6×10^3 Schwarzschild radii (R_s) during the high-energy active state. This result is a contrast to another case of the astrometric observation of the famous nearby TeV blazar Mrk 421, which showed a clear radio core position change soon after the large X-ray flare in 2011, reported by Niinuma et al. We compare the two cases and discuss possible origins of the different results of the radio core astrometry in the high-energy active states between the nearby blazars. Based on the internal shock model for blazars, the Lorentz factors of the ejecta explaining the stability of the radio core in Mrk 501 are expected to be a few times smaller than those for the wandering core in Mrk 421.

Key words: BL Lacertae objects: individual (Mrk 501) – galaxies: active – galaxies: jets

1. Introduction

Blazars are active galactic nuclei (AGNs) with jets of nonthermal plasma moving at relativistic speeds oriented close to our line of sight. It is well known that they produce nonthermal radiation across the electromagnetic spectrum from radio to γ-rays. Probing the location of the emission region with respect to the central engine is one of the most fundamental topics for understanding emission mechanisms in relativistic jets in AGNs. Regarding the nonthermal radio emissions from blazars, one of the leading scenarios suggests that the radio cores in blazars correspond to stationary shocked regions located several parsecs downstream of the central engine based on the indirect estimation of the delay timescale between the precedent γ-ray flares and the radio core brightening (e.g., Marscher et al. 2008; Jorstad et al. 2017). On the contrary, the radio cores in radio galaxiescorrespond to the surface where the optical depth becomes unity for synchrotron self-absorption at each frequency, located farther upstream of the jets. High-precision radio core astrometry has been intensively performed toward the nearby radio galaxy M87 (e.g., Hada et al. 2011, 2014), showing that the 43 GHz radio core is located ~0.01 pc from the central engine and stable within ~300 μas. Therefore, it is important to further explore the discrepancy of the radio core locations between radio galaxies and blazars, by performing direct astrometric observations toward the blazars' radio cores.

For directly probing the locations of radio cores in blazars, VLBI astrometric observations are the most reliable method. Especially for the two nearby representative TeV blazars Mrk 421 and Mrk 501, since the radio cores usually show a convex shape spectrum peaking around ~10 GHz (Giroletti et al. 2008; Sokolovsky et al. 2010; Lico et al. 2012; Blasi et al. 2013), the radio cores can be regarded as the internal shocked regions (e.g., Spada et al. 2001; Tanihata et al. 2003; Guetta et al. 2004; Kino et al. 2004; Ghisellini et al. 2005). Therefore, observing the radio cores at higher frequencies (equal to or higher than ~22 GHz) would correspond to seeing through the internal shocked regions. Their proximity and the availability of nearby phase calibrators also enabled astrometric observations. As a recent interesting example, the radio core in the blazar Mrk 421 significantly changes its location toward ~500 μas downstream within a few months and changes back

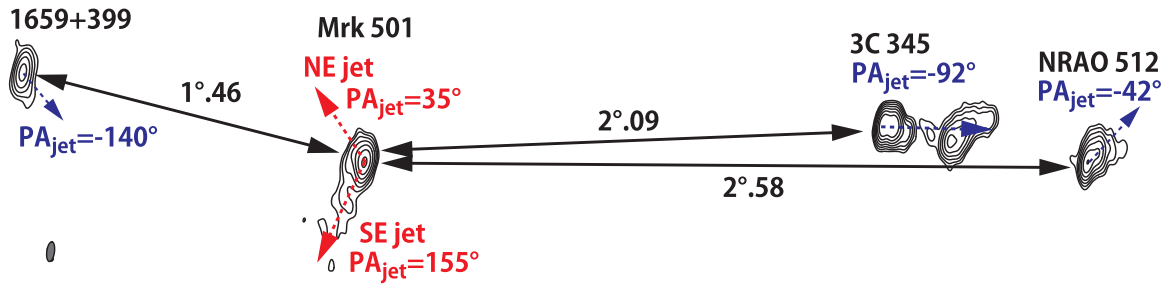

Figure 1. Source configuration on the sky plane, and the self-calibrated images of the third epoch. Contours start at the 3σ level, increasing by factors of 2. The typical beam size of the observations is shown at the lower left. The beam size and the 1σ level for each source are summarized in Table 2. The dotted red arrows indicate the direction of the northeast (NE) jet component and the averaged position angle of the southeast (SE) jet components of Mrk 501. The dotted blue arrows indicate the direction of the jet component next to the radio core for the other sources.

to its initial location around half a year after that, from the dense monitoring of the radio core positions with VLBI Exploration of Radio Astrometry (VERA) following its large X-ray flare in 2012 September (Niinuma et al. 2015). The pilot astrometric study toward Mrk 501 with the VERA at 43 GHz has also been performed, and the radio core position did not show clear position offsets, located within 200 μas during its quiescent state between 2011 February and October (Koyama et al. 2015). However, since the astrometric observations toward the two blazars were performed during different states, and also the two-epoch observations for Mrk 501 were not enough to discuss the time evolution, it was difficult to compare the astrometric results between these two blazars. Thus, higher-cadence astrometric observations toward Mrk 501 during their high-energy active states are needed to compare the results of the two TeV blazars and search for any relation between the position of the radio cores and their activities.

From 2011 November to 2012 August, Mrk 501 went into its active state in X-rays (with *Swift*/XRT, *Swift*/BAT, and MAXI; Sootome et al. 2011; Bartoli et al. 2012; Kapanadze et al. 2017; Ahnen et al. 2018). A large TeV γ-ray flare at 5 crab above 1 TeV was reported on 2012 June 9 (with MAGIC and FACT; Ahnen et al. 2018), by following a peak on 2011 November 8 (with ARGO-YBJ; Bartoli et al. 2012), which seems to be correlated with X-ray flares. Especially, the very high energy (VHE; $E > 0.1$ TeV) flare is one of the largest flares, comparable to the historical flares in 1997 (e.g., Catanese et al. 1997; Pian et al. 1998; Aharonian et al. 1999), and also the average flux above 1 TeV from 2012 March until August was $\sim$1 crab, which is about three times as high as the typical flux of the nonflaring state. Therefore, it is a good opportunity to study whether the radio core position of Mrk 501 changes or not for the first time during its high-energy (X-ray and/or VHE γ-ray) active state, as is detected in Mrk 421. We performed the precise astrometric observations toward Mrk 501 at 43 GHz with the Very Long Baseline Array (VLBA) for the first time during these X-ray and VHE γ-ray active states over six epochs spanning 1 yr from 2012 to 2013 February for compensating the number of observing epochs. From these observations, Koyama et al. (2016) have already reported the details of the jet structure, as well as the angular separation and position angle of individual components relative to the core, by assuming that the core position is stationary, not from the perspective of the astrometry. In this paper, we revisit the same data set and report the results of the analysis of the astrometric part to study the radio core positions during its high-energy active state and search for any relation between the position of the radio cores and the high-energy activities in the two blazars. In Section 2 we describe the observations, in Section 3 we describe the data reduction, and in Section 4 we present the astrometric results. In Section 5 we discuss the results in comparison with the case of Mrk 421, together with its high-energy activities, and the possible origin of the jet in Mrk 501. Throughout this paper, we adopt the following cosmological parameters: $H_0 = 71$ km s^{-1} Mpc^{-1}, $\Omega_M = 0.27$, and $\Omega_\Lambda = 0.73$, or 1 mas = 0.66 pc for Mrk 501 ($z = 0.034$).

2. Observations

The astrometric observations with the VLBA have advantages compared to our previous ones with VERA (Koyama et al. 2015), since the VLBA has longer baselines than the VERA[16] by a factor of about four (up to 8600 km), and the baseline sensitivity is improved by the larger collecting surface and higher antenna efficiency of the dishes. The smaller beam size reduces the main positional error due to the source structure effect, and the higher baseline sensitivity enables us to use fainter and closer calibrators. More antennas also enable us to get a much-enhanced *uv*-coverage and better data constraints owing to the larger number of closures in phase and amplitude.

Our six-epoch observations were performed between 2012 and 2013 February with the VLBA in astrometric mode. The self-calibrated images and the related discussions of Mrk 501 from these observations have already been reported in Koyama et al. (2016). The observing details (dates, codes, and station information) can be found in Table 1 in Koyama et al. (2016). The observations include rapid switching within 30 s between Mrk 501 and three nearby radio sources: 3C 345 ($z = 0.593$), NRAO 512 ($z = 1.66$), and 1659+399 ($z = 0.507$). The alignment of the sources on the sky plane is shown in Figure 1, together with contour plots of the parsec-scale images. Left-hand circular polarization was recorded at the central frequency of 43.212 GHz. The data recording speed was 512 Mbps, with a total bandwidth of 128 MHz (eight sub-bands of 16 MHz). Data was correlated by the VLBA-DiFX software correlator (Deller et al. 2011). The delay-tracking center of all the observed sources is summarized in Table 1. The three sources, Mrk 501, 3C 345, and NRAO 512, were observed with the same coordinates as those used in the VERA astrometric observations (Koyama et al. 2015), and this time the new faint source 1659+399 was added for a consistency check.

The total observation time was 4 hr per epoch, in which the total net on-source time was approximately 1 hr for Mrk 501, half an hour for 3C 345 and NRAO 512, and the rest ($\lesssim$2 hr) was the antenna slewing time. The new faint source 1659+399

[16] https://www.miz.nao.ac.jp/veraserver/restricted/CFP2011/status11.pdf

Table 1
The Delay-tracking Center of the Observed Sources

Source Name (1)	R.A. (2)	Decl. (3)
Mrk 501	$16^h53^m52^s.216685$	$+39°45'36''.60894$
3C 345	$16^h42^m58^s.809965$	$+39°48'36''.99399$
NRAO 512	$16^h40^m39^s.632772$	$+39°46'46''.02849$
1659+399	$17^h01^m24^s.634816$	$+39°54'37''.09159$

Note. All the coordinates (J2000.0) in right ascension (R.A.) and in declination (decl.) were taken from the International Celestial Reference Frame 2 (ICRF2; Fey et al. 2009).

was observed three times at the beginning, in the middle, and at the end of each epoch from the first to fourth epoch as a test basis, because the source flux at 43 GHz was unknown. From the fifth epoch, this source was observed six times with a few scans spread over each epoch. Since each on-source time was around 13 s in the case of 25 s switching time, the net on-source time for 1659+399 was 2–4 minutes per epoch. Therefore, the data of this source were used for the consistency check.

3. Data Reduction

The initial data calibration was performed using the Astronomical Image Processing System (AIPS), based on the standard VLBI data reduction procedures. The Earth orientation parameters were corrected by using the AIPS task VLBAEOPS, and the ionospheric dispersive delays were corrected with VLBATECR by using the ionospheric model provided by the Jet Propulsion Laboratory (JPL). The parallactic angle difference among calibrators and targets was corrected by using CLCOR with the parameter PANG. The amplitude calibration with the opacity corrections was applied by using the measured system noise temperature and the elevation gain curve of each antenna. The instrumental delays and phases were solved by using a scan of the brightest source 3C 345. We performed a fringe fitting on all four sources and removed residual delays, rates, and phases by assuming a point-source model. We obtained the source structure phases due to the deviation from the point-source model by iterative clean and self-calibration procedures and obtained the clean component models (CC models) for them. Since 1659+399 is close to the detection threshold of VLBA at 43 GHz and only a few scans were allocated, the fringe solutions were less reliable. Therefore, we applied the fringe solutions of Mrk 501 to 1659 +399 and then performed clean self-calibration on it to obtain its CC models. The self-calibrated image parameters are summarized in Table 2. By performing a fringe fitting again by including the CC models for each source, the CC models were directly Fourier transformed and subtracted from the observed visibilities. In the standard phase-referencing data reduction, after the calibrator phases and the target gain time variability assigned to atmosphere or instrumental effects are applied to each target, phase-referenced images were created, and the peak positions of the phase-referenced images were measured by fitting a single Gaussian to the peak component using the AIPS task JMFIT. If the structure of each target source is close to a point source, this standard procedure can be used to derive the phase-referenced peak position.

In the case of these VLBA 43 GHz observations, the peak position measurement would include non-negligible component identification errors, because all the sources have extended source structure with this spatial resolution (typically 0.45 mas × 0.14 mas), while they were close to point sources or very simple with the VERA resolution (typically 0.67 mas × 0.40 mas at 43 GHz). Therefore, we performed the new data reduction procedure to carefully remove the phase of the source structure for both of the targets and the calibrators by writing down the phase terms of the observing equations, which are summarized in Appendix A. At first, we chose Mrk 501 as a phase calibrator (C1) and transferred the derived fringe solutions including its CC model (ϕ_{SN1}^{C1}) to all the other targets (T = 3C 345, NRAO 512, and 1659 + 399, respectively; see Equation (7)), since Mrk 501 is bright enough to perform fringe fitting and self-calibration (Equation (5)). The method performs the subtraction of the visibility amplitudes and phases of the target source structure, which were previously obtained through self-calibration, from the phase-referenced visibilities to make the solution table SN2 (Equation (8)). Separately, we produced the model visibilities of a single point source with the total flux density of the target at the phase center (0, 0) by using the AIPS task CALIB. By applying SN2 to the point-source visibilities, we obtained phase-referenced images for the three targets (3C 345, NRAO 512, and 1659+399). These images did not include the amplitude and phase components of source structures, but of astrometric positions and all of the calibration errors. After this new reduction procedure, signal-to-noise ratios of the phase-referenced images were improved a few times as high as those with the standard phase-referencing procedure, and it helped us to identify the peak positions in the images (see more details in Section 4.1).

The peak position offsets from the phase-tracking center on the phase-referenced images were measured with the AIPS task JMFIT because the signal-to-noise ratios of the visibilities were low. The peak positions were also confirmed by model fitting to the phase-referenced visibilities and are consistent with those by JMFIT typically within ∼10 μas, less than ∼30 μas. Our goal is to derive the relative position of the radio core positions between the targets and the calibrator. We considered that the JMFIT peak position in the phase-referenced image corresponds to the model-fitted peak position in the self-calibrated image, which usually corresponds to the position of the radio core. We derived the radio core positions by subtracting from the JMFIT peak positions of the phase-referenced images the peak position differences between the JMFIT peak positions of the self-calibrated images and the core positions obtained from model fitting to the self-calibrated visibilities (defined as core identification errors, which are typically a few μas, less than ∼10 μas except for NRAO 512, shown in Table 4 in Appendix B), and subtracting the position offsets of the model-fitting radio core position from the phase center in the self-calibrated images. As for 3C 345, at the fourth and sixth epochs, the peak positions in the self-calibrated images did not correspond to the radio core, which is the easternmost compact component labeled as Q0 in Schinzel et al. (2012). Except for these, we defined the brightest component in each image as the radio core. Since the relative positions between calibrators and targets are conserved, the phase-referenced position of Mrk 501 with respect to the three targets is derived by multiplying −1 by the measured positions

Table 2
Self-calibrated Image Parameters for All Four Sources

Source	Epoch	Beam Size			I_p	σ_{rms}	I_p/σ_{rms}	F_{tot}
		(mas)	(mas)	(deg)	(mJy beam^{-1})	(mJy beam^{-1})		(mJy)
(1)	(2)	(3)	(4)	(5)	(6)	(7)	(8)	(9)
Mrk 501	2012 Feb 12	0.47	0.12	−22.4	209	1.13	185	377
	2012 Mar 16	0.32	0.11	−13.5	178	0.72	248	356
	2012 May 6	0.31	0.12	−7.59	209	0.94	224	453
	2012 Jun 11	0.34	0.17	12.8	249	1.17	214	476
	2013 Jan 18	0.34	0.12	−17.5	120	0.66	183	266
	2013 Feb 15	0.33	0.13	−27.4	130	0.70	186	298
3C 345	2012 Feb 12	0.45	0.12	−22.8	947	2.36	401	2760
	2012 Mar 16	0.35	0.12	−16.9	933	1.90	492	3040
	2012 May 6	0.30	0.11	−8.35	1130	2.22	511	3840
	2012 Jun 11	0.35	0.17	14.3	1800	3.40	530	4190
	2013 Jan 18	0.36	0.12	−21.5	887	1.29	690	2940
	2013 Feb 15	0.31	0.12	−23.8	974	1.73	564	2990
NRAO 512	2012 Feb 12	0.44	0.12	−22.6	278	1.56	178	505
	2012 Mar 16	0.34	0.12	−16.1	248	1.64	151	515
	2012 May 6	0.31	0.12	−8.28	307	1.60	192	673
	2012 Jun 11	0.36	0.17	12.9	323	2.48	130	659
	2013 Jan 18	0.35	0.12	−21.3	282	1.29	218	586
	2013 Feb 15	0.33	0.12	−26.6	234	1.26	185	514
1659+399	2012 Feb 12	0.52	0.15	−18.9	137	3.62	38	138
	2012 Mar 16	0.41	0.15	−14.7	91.5	2.42	38	120
	2012 May 6	0.39	0.15	−9.53	161	2.45	66	198
	2012 Jun 11	0.38	0.19	11.28	157	4.38	36	194
	2013 Jan 18	0.41	0.14	−19.8	105	1.52	69	129
	2013 Feb 15	0.48	0.20	−27.4	102	1.73	59	112

Note. Columns are as follows: (1) source; (2) observing epoch; (3) major-axis size of the synthesized beam; (4) minor-axis size of the synthesized beam; (5) position angle of the synthesized beam; (6) peak intensity; (7) image rms noise; (8) peak over rms; (9) total cleaned flux. The images of Mrk 501 were slightly improved with the same data set in Koyama et al. (2016).

in R.A. and decl. As for the cross-check of this phase-referencing, we also performed the phase-referencing inversely by fringe fitting on bright calibrators 3C 345 and NRAO 512, including their CC models, and apply the solutions to Mrk 501.

As is shown in Figure 1, since all the sources show the resolved jet structure with the VLBA at 43 GHz, the observed radio core position differences of Mrk 501 in the phase-referenced images would be the mixture of the possible radio core wandering of the other sources. We assume that the direction of the possible core wandering is related to the direction of the jet and its flux ratio with respect to the total cleaned flux. Therefore, first, we performed Gaussian model fitting to the self-calibrated visibilities of Mrk 501. In Koyama et al. (2016), the new component located ∼0.18 mas northeast of the radio core was found, labeled NE by performing circular Gaussian model fitting. This time elliptical Gaussian models are fitted at the radio core of Mrk 501 to trace the brightest peak positions, yet the locations of the jet components did not significantly change from those fitted with circular Gaussians in Figure 10 of Koyama et al. (2016). Mrk 501 is always core dominant, and the core dominance (radio core flux over the total cleaned flux) is 0.6–0.7. Since the sums of the component fluxes at the northeast of the core and at the southeast are usually very similar, we defined the two representative jet axes for Mrk 501 by averaging the position angles of the jet components over all the epochs; one is for the NE jet component at 35°, and the other one is for the SE jet using all the SE components at 155° (Figure 1). Second, we performed circular Gaussian model fitting to the self-calibrated visibilities of the other sources. Elliptical Gaussian fitting did not improve the fitting results for them. Thus, we derived the jet position angle of 3C 345, NRAO 512, and 1659+399 as their representative jet axes, at −92°, −42°, and −140°, respectively, by averaging over all the epochs the position angles of the components next to the radio cores. The standard deviations of the jet position angles were typically within several degrees. After deriving the peak positions of the phase-referenced images of 3C 345, NRAO 512, and 1659+399 relative to Mrk 501's core, we projected the positions orthogonal to their jet position angles and recalculated them along the SE or NE jet of Mrk 501 (Section 4.2).

4. Results

4.1. Phase-referenced Image Qualities

In Table 3, the image qualities of the phase-referenced images and the core positions are summarized. The final phase-referenced images of 3C 345, NRAO 512, and 1659+399 relative to Mrk 501 core are shown in Figure 8 (Appendix B). Since we reduced the effect of the source structures for both calibrators and targets as much as we can with the new reduction procedure, the phase-referenced images appear as a point-like source with some scattered emission. These scatterings of phase-referenced images come from the thermal noise and various calibration errors. For all the epochs, all the targets are detected with image signal-to-noise ratios higher than 14, which are about a few times higher than those with the standard phase-referencing procedure. The high signal-to-noise ratio in the phase-referenced images enables us to identify the peak positions more easily. It improves the random errors, which is

Table 3
Image Qualities of Phase-referenced Images and Core Positions of Mrk 501

Phase-referenced Pair	Epoch	I_p (mJy beam^{-1})	σ_{rms} (mJy beam^{-1})	I_p/σ_{rms}	$\Delta\alpha$ (mas)	$\Delta\delta$ (mas)
(1)	(2)	(3)	(4)	(5)	(6)	(7)
Mrk 501−3C 345	2012 Feb 12	2310	102	23	−0.455 ± 0.051	−0.469 ± 0.052
	2012 Mar 16	2280	93.7	24	−0.411 ± 0.050	−0.420 ± 0.051
	2012 May 6	3040	111	27	−0.408 ± 0.049	−0.512 ± 0.050
	2012 Jun 11	3420	169	20	−0.482 ± 0.050	−0.441 ± 0.051
	2013 Jan 18	2040	73.0	28	−0.459 ± 0.052	−0.431 ± 0.051
	2013 Feb 15	2180	109	20	−0.575 ± 0.050	−0.423 ± 0.050
Mrk 501−NRAO 512	2012 Feb 12	387	22.3	17	0.020 ± 0.066	−0.083 ± 0.075
	2012 Mar 16	366	19.4	19	0.040 ± 0.069	−0.067 ± 0.083
	2012 May 6	513	25.9	20	0.024 ± 0.061	−0.084 ± 0.064
	2012 Jun 11	534	32.0	17	0.018 ± 0.062	−0.023 ± 0.064
	2013 Jan 18	415	21.6	19	−0.052 ± 0.065	0.013 ± 0.065
	2013 Feb 15	375	22.9	16	0.039 ± 0.061	0.010 ± 0.063

Note. Columns are as follows: (1) phase-referencing pair; (2) observing epoch; (3) peak intensity of the phase-referenced image; (4) image rms noise; (5) signal-to-noise ratio of the image; (6, 7) position offset from phase-tracking center for Mrk 501.

estimated to be inversely proportional to the signal-to-noise ratio (Columns (3) and (4) of Table 4 in Appendix B). It does not improve the total core position errors since they are dominated by tropospheric zenith delay error (see the typical values in the next subsection). The flux loss ratio can be evaluated by comparing the peak fluxes of the phase-referenced images (Column (3) of Table 3) to the total cleaned fluxes of the self-calibrated images (Column (9) of Table 2), because a single point-source model with the total cleaned flux was created at the phase center and shifted to the phase-referenced position. The averaged flux loss ratio is 84% for 1659+399, 77% for 3C 345, and 75% for NRAO 512.

4.2. Core Peak Position of Mrk 501 Relative to 3C 345 and NRAO 512

In Table 3, the core positions of Mrk 501 relative to the radio core positions of 3C 345 and NRAO 512 are summarized. The core position errors are estimated as the root sum square of each error (see Appendix B). The measurements are plotted in Figures 2(a) and 3(a). The position offsets of Mrk 501 are extracted along the perpendicular direction to the jet position angles of 3C 345 and NRAO 512 (blue arrows) and recalculated along the SE or NE jet of Mrk 501 (red arrows). We chose the combination of the jet direction of Mrk 501 (SE or NE) and that of 3C 345 and NRAO 512 to have more nearly perpendicular position angle difference. As for the position offsets along the SE jet, we use the phase-referencing pair of Mrk 501 and 3C 345 (Figure 2(a)). For the positional offsets along the NE jet, we use the phase-referencing pair of Mrk 501 and NRAO 512 (Figure 3(a)), because the direction of possible core wandering of NRAO 512 is close to that of the SE jet of Mrk 501. The recalculated core positions of Mrk 501 along each jet are plotted in Figures 2(b) and 3(b). The phase-referencing pair of Mrk 501 and 1659+399 was used for the confirmation and the results are presented in Table 5 (Appendix C).

4.2.1. Core Peak Positions of Mrk 501 Relative to 3C 345

Figure 2(a) shows that all the measured core positions of Mrk 501 relative to the core positions of 3C 345 are located within a small region. The core position error is estimated to be 50 μas in R.A. and 52 μas in decl. on average, which is around 1/10 of the major axis of the synthesized beam size. The major error contribution comes from the tropospheric zenith delay errors, which are typically ∼3 cm for the VLBA (Reid et al. 1999), corresponding to the position error of ∼49 μas for the separation of 2°.09 between Mrk 501 and 3C 345. The signal-to-noise ratios of the phase-referenced images range from 20 to 28, which is the highest among all the phase-referencing pairs, thanks to its highest brightness.

Figure 2(b) shows the recalculated core positions of Mrk 501 along its SE jet relative to the core positions of 3C 345. We performed a *t*-test of the core positions over the six epochs for the evaluation of its stationarity. The core positions of Mrk 501 relative to 3C 345 coincide along the position angle of the SE jet with the significance probability of 69%. The weighted-mean position and error along the SE jet is −22 ± 21 μas. Therefore, we conclude that the phase-referenced core peak positions of Mrk 501 relative to 3C 345 lie within 42 μas ($\pm1\sigma$) along the SE jet direction. The core positions of Mrk 501 along the SE jet were confirmed by using 1659+399, and a similar significance probability of the stationarity was obtained (Appendix C).

4.2.2. Core Peak Positions of Mrk 501 Relative to NRAO 512

Figure 3(a) shows the measured core positions of Mrk 501 relative to the peak positions of NRAO 512. The core position error is estimated to be 64 μas in R.A. and 70 μas in decl. on average. The tropospheric zenith delay errors correspond to the position error of ∼60 μas for the separation of 2°.58 between Mrk 501 and NRAO 512. The signal-to-noise ratios of the phase-referenced images range from 16 to 20.

Figure 3(b) shows the recalculated core positions of Mrk 501 along its NE jet relative to the core positions of NRAO 512. From a *t*-test of the core positions over the six epochs, the core positions of Mrk 501 relative to NRAO 512 coincide along the position angle of the NE jet of Mrk 501 with the significance probability of 95%. The weighted-mean position and error along the NE jet is 27 ± 27 μas. Thus, we can conclude that the phase-referenced core peak positions of Mrk 501 relative to NRAO 512 lie within 53 μas ($\pm1\sigma$) along its jet direction.

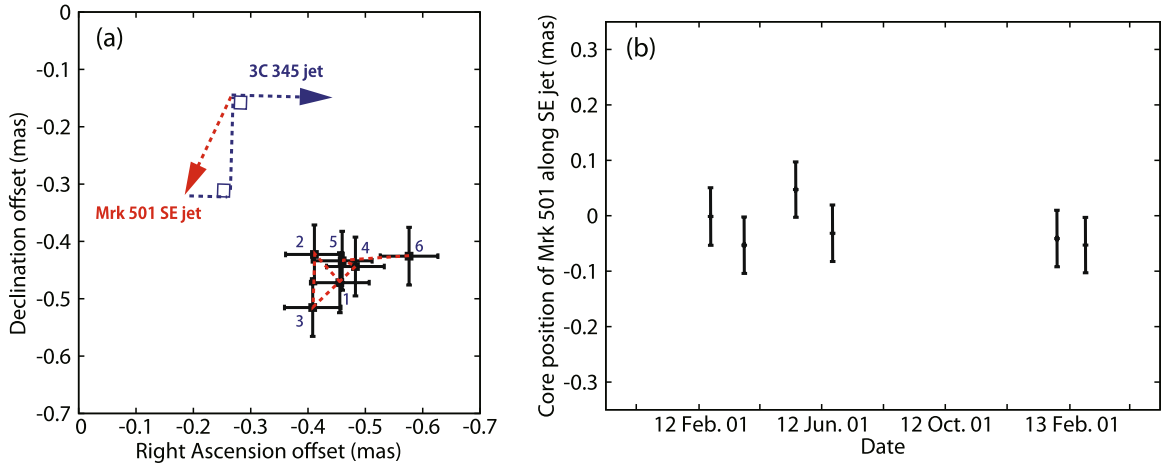

Figure 2. Measured radio core position of Mrk 501 relative to the radio core of 3C 345. (a) The horizontal and vertical axes show the positional offsets of R.A. and decl. from the observation coordinates with 1σ positional uncertainties. The numbering represents the order of the observation epochs. The blue arrows indicate the jet direction of 3C 345, and the red arrows indicate the SE jet direction of Mrk 501. (b) The horizontal and vertical axes show the time and the positional offsets along the direction of Mrk 501's SE jet with respect to the position of the first epoch. The positional offsets are extracted along the perpendicular direction to the jet of 3C 345 and recalculated along the SE jet direction of Mrk 501. The core positions are shifted as epoch 1 corresponding to 0 in y-axis.

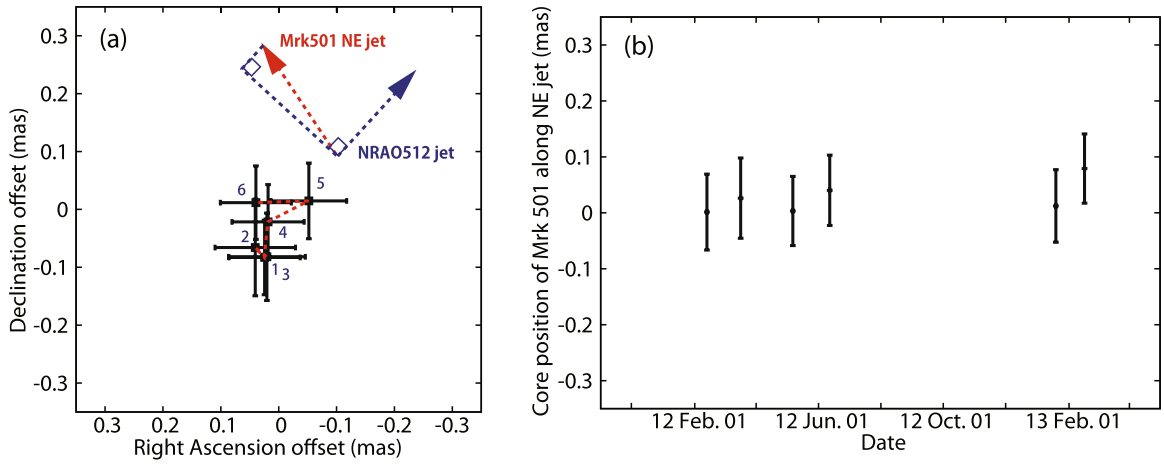

Figure 3. Measured radio core position of Mrk 501 relative to the radio core of NRAO 512, as is shown in Figure 2. (a) The blue arrows indicate the jet direction of NRAO 512, and the red arrows indicate the direction of Mrk 501's NE jet. (b) The horizontal and vertical axes show the time and the positional offsets along the jet direction of Mrk 501's NE jet with respect to the position of the first epoch. The positional offsets are extracted along the perpendicular direction to the jet of NRAO 512 and recalculated along the NE jet direction of Mrk 501.

4.3. Radio Core Astrometry with the VERA and the VLBA

In Figure 4, the position errors measured with the VERA in 2011 February and October (gray cross) and those with the VLBA during this time (red cross) are shown at the origin of the self-calibrated image. The phase-referenced core positions determined by the VLBA are well refined and concentrated on the brightness peak position, not scattering over the other components. The position accuracy with the VERA, which was 200 μas averaged over four successive days, was improved around four times by the VLBA mainly owing to its higher resolution, being 42 μas or 4.6×10^3 Schwarzschild radii (R_s) deprojected in the direction of the SE jet, and 53 μas in the NE jet direction over 1 yr. Here, a resolution of 100 μas corresponds to $7.7 \times 10^2 R_s$ projected and $1.1 \times 10^4 R_s$ deprojected for a lower limit of the jet viewing angle of $\theta_j = 4^\circ$ (Giroletti et al. 2004), with the minimum of the central black hole mass of Mrk 501 being $M_{BH} = 0.9 \times 10^9 M_\odot$ (lower limit in Barth et al. 2002, the value used in Koyama et al. 2015).

We further compare the phase-referenced core positions between the VERA measurements and the VLBA measurements, since the same source coordinates are used for Mrk 501, NRAO 512, and 3C 345 for both observations. Note that the nonidentical arrays and the different observing epochs (2 yr at maximum) may introduce some systematic errors.

4.3.1. Core Peak Positions of Mrk 501 Relative to NRAO 512

Figure 5 shows the phase-referenced core positions of Mrk 501 relative to the radio core of NRAO 512 measured with the VLBA (black crosses) and with VERA (blue and red crosses). The phase-referenced core positions of Mrk 501 are all within the error bars over the 2 yr and do not show significant offsets. The radio core positions for all the epochs including the errors are located within $\sim$300 μas, and the peak positions are located within $\sim$200 μas.

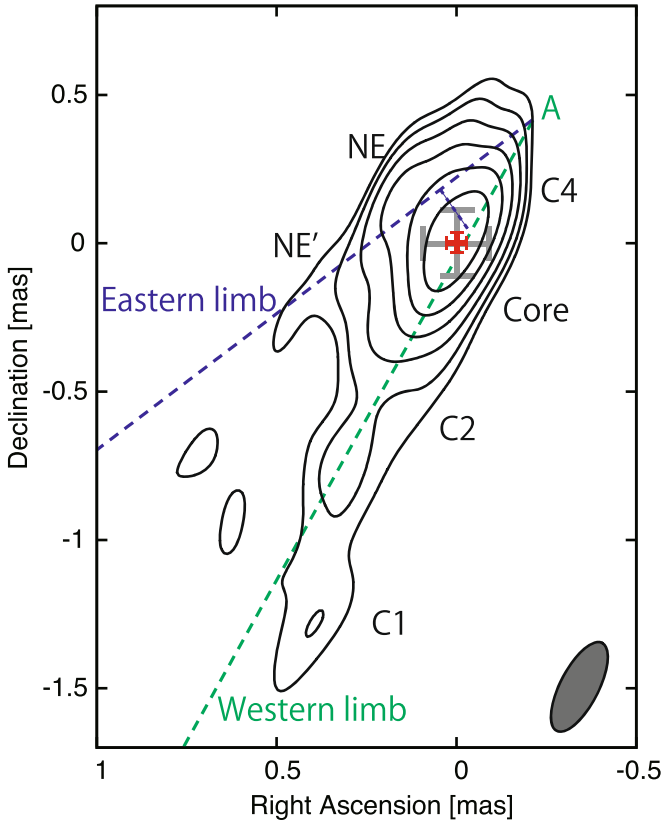

Figure 4. The contour map shows the self-calibrated image for the sixth epoch. Since the phase-referenced radio core position was stable, the radio core position is set to its map origin as (0, 0). Position errors averaged over four successive days with the VERA (200 μas; gray cross) and over 1 yr with the VLBA (42 μas in the southeast and 53 μas in the northeast; red cross) are shown at (0, 0) of the image. The beam size of the self-calibrated image is shown at the lower right. We define the dotted blue line as the eastern limb from the least-squares fitting to the components NE and NE′, and the dotted green line fitted to the radio core and the components C1, C2, and C4 as the western limb.

4.3.2. Core Peak Positions of Mrk 501 and NRAO 512 Relative to 3C 345

Figure 6(a) shows the phase-referenced core positions of Mrk 501 relative to 3C 345, and Figure 6(b) shows those of NRAO 512 relative to 3C 345 for both the VERA and VLBA measurements. We find that the core positions measured with the VLBA are clearly different from those measured with the VERA. If it is physical position offset, these results indicate that the core positions of 3C 345 change around 300 μas at a position angle of $24^{+14}_{-6.7}$ deg relative to Mrk 501 and $30^{+5.6}_{-4.4}$ deg relative to NRAO 512, by assuming that the core positions of Mrk 501 and NRAO 512 are stationary. The position angles are consistent with each other. The position angle of the 3C 345 −NRAO 512 pair is also consistent with the position angle derived only by using the VERA observations (36^{+24}_{-27} deg; Koyama et al. 2015). However, the VLBA-only data do not show significant position change, such that this may imply variable core position change. Figure 2 in Bartel et al. (1986) also shows similar direction of the positions of 3C 345 core relative to NRAO 512 over the first year, although they claim that the proper motions of the core are not significantly different from zero over 11 yr. The difference between the direction of the possible position change and the position angle of 3C 345 jet was already pointed out in Koyama et al. (2015),

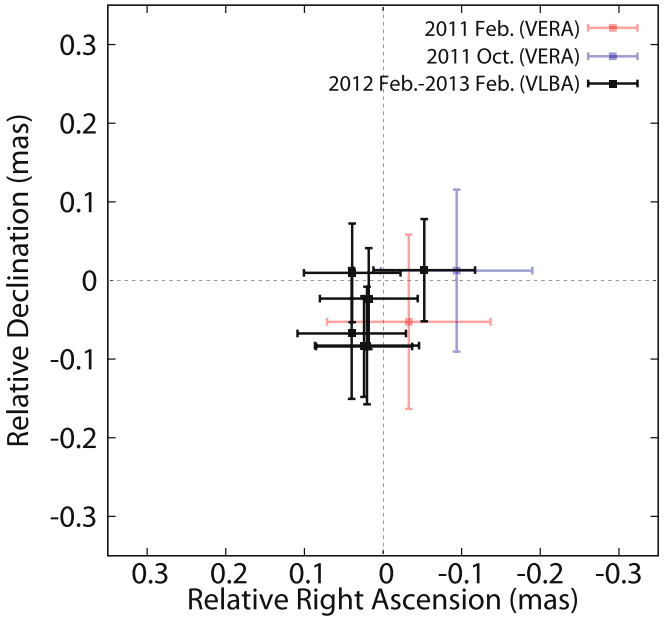

Figure 5. Radio core position of Mrk 501 relative to the radio core of NRAO 512, measured with the VLBA for each epoch (black crosses, same as Figure 3), and with the VERA averaged over four successive measurements in 2011 February and October (red cross and blue cross, respectively, taken from Figure 3 in Koyama et al. 2015).

and it became clearer by including these VLBA measurements, being around 128°. Therefore, it cannot be explained only by the emergence of the new component along its jet, and it could be related to wandering of the jet origin itself (e.g., Agudo 2009). The possible position shift of 3C 345 core will be further investigated with our continued astrometric observations with the VLBA.

5. Discussion

5.1. Comparison of the Radio Core Positions and the High-energy Activities between Mrk 501 and Mrk 421

We performed the precise astrometric observations toward the radio core of Mrk 501 for the first time during its active states at both X-rays and VHE γ-rays, which includes the VHE flare in 2012. Although the first four epochs were performed during the active states, the astrometric results show stable radio core positions within 42 μas or $4.6 \times 10^3\,R_s$ deprojected along the SE jet direction. On the other hand, the astrometric observations toward the radio core of Mrk 421 revealed a clear position offset of ∼500 μas along its jet axis, or a few times $10^5\,R_s$ deprojected ($M_{BH} = 3.6\times 10^8\,M_\odot$; Wagner 2008), soon after its giant X-ray flare in 2011 September (Niinuma et al. 2015). The projected distribution scale of the radio core of Mrk 501 is estimated to be about 1/10 of the amount of the core wander of Mrk 421, and the deprojected scale in R_s is about 1/30 that of Mrk 421 (the estimated black hole mass of Mrk 501 is about three times as heavy as that of Mrk 421 with similar jet viewing angle). Here we discuss possible origins of the differences between the two representative TeV blazars based on the standard internal shock model and on the characteristics of the spectrum in X-rays and/or VHE γ-rays.

First, we discuss the discrepancy of the distribution scale of the radio core positions based on the discussions of the internal shock model (Koyama et al. 2015; Niinuma et al. 2015). As is discussed there, the radio cores in Mrk 501 and Mrk 421

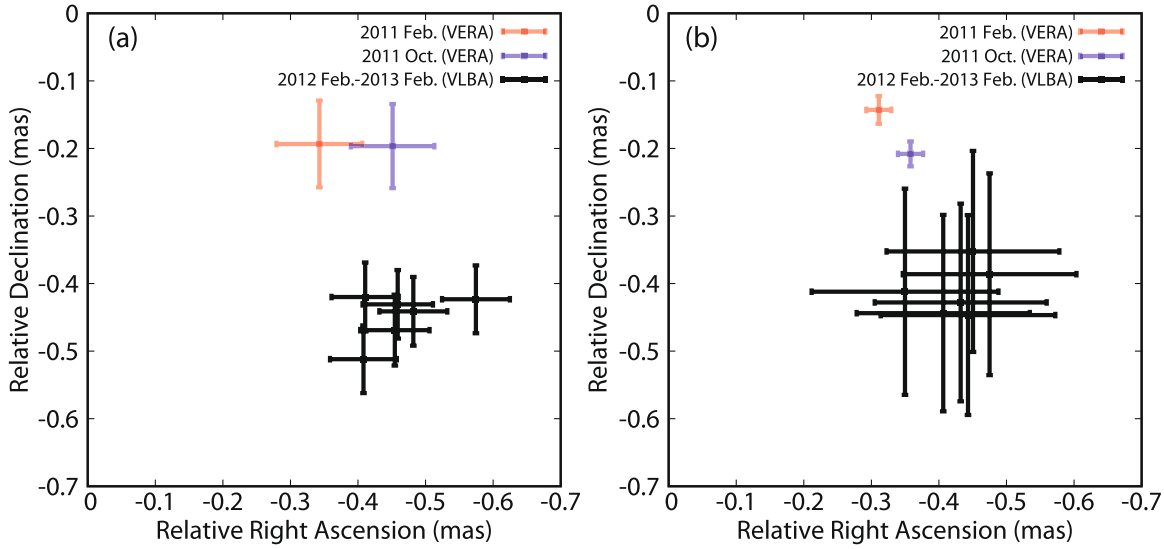

Figure 6. (a) Core positions of Mrk 501 relative to 3C 345's core. The positions measured with the VLBA are the same as those in Figure 2. (b) Core positions of NRAO 512 relative to 3C 345's core. The positions measured with the VLBA are obtained by subtracting the core positions in Figure 5 from those in Figure 6(a). The VLBA measurements are shown as black crosses, and the VERA measurements are shown as red and blue crosses, which are averaged over four successive measurements in 2011 February and October, taken from Figures 4(a) and (b), respectively, in Koyama et al. (2015).

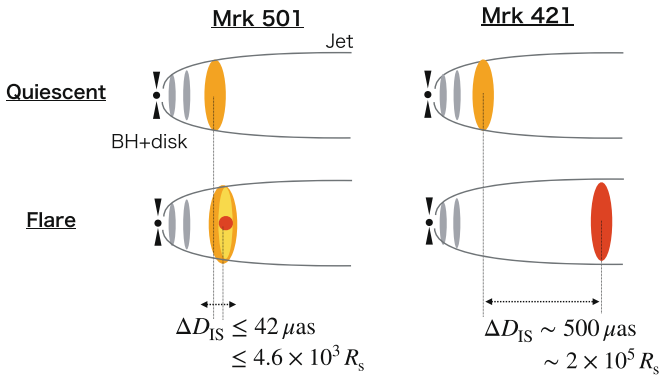

Figure 7. Schematic picture of the results of the radio core astrometry toward Mrk 501 and Mrk 421 during their quiescent state and flaring state. We consider the radio cores that correspond to the internal shock emitting region as orange or red blobs, where the faster ejecta catch up with slower ejecta. $\Delta D_{\rm IS}$ represents the difference of the distance of the internal shocked regions and the central engine ($D_{\rm IS}$) between quiescent and high-energy active states. Left: for Mrk 501, during its quiescent states usually radio to VHE γ-ray emission can be explained with the one-zone SSC model (orange blob). During this EHBL state in 2012 (Ahnen et al. 2018), it requires a smaller TeV γ-ray flaring zone (red blob), an averaged larger zone dominating optical to MeV emission (yellow blob), and the remaining zone dominating radio emission (orange blob), by assuming that they are located close to each other. Right: in the case of Mrk 421, the emission from radio to VHE γ-rays can be explained with the one-zone SSC model at both quiescent states (orange blob) and the flaring state (red blob).

observed at 43 or 22 GHz can usually be considered as the internal shocked regions owing to the convex shape of the radio spectrum peaking around 10 GHz (Giroletti et al. 2008; Sokolovsky et al. 2010; Lico et al. 2012; Blasi et al. 2013). The standard internal shock model of blazars considers that the discrete ejecta with higher speeds (with Lorentz factor $\Gamma_{\rm f}$) catch up with the preceding slower ejecta (with Lorentz factor $\Gamma_{\rm s}$), and the collision leads to the nonthermal emission (e.g., Spada et al. 2001; Tanihata et al. 2003; Guetta et al. 2004; Kino et al. 2004; Ghisellini et al. 2005). Based on the model, the distribution scale of the internal shocks ($\Delta D_{\rm IS}$ in Figure 7, defined as the difference between the largest distance between the internal shock and the central engine $D_{\rm IS,max}$ and the closest one $D_{\rm IS,min}$) can be explained as the variation of the Lorentz factors of the ejecta (Koyama et al. 2015; Niinuma et al. 2015), by assuming the Lorentz factor ratio ($\Gamma_{\rm f}/\Gamma_{\rm s}$) and the initial separation of the ejecta ($I_{\rm IS}$). The core stable within 200 μas constrained by the VERA can be explained by Lorentz factors within a factor of two variation for the slower ejecta, i.e., $8 \leqslant \Gamma_{\rm s} \leqslant 17$, by assuming a minimum value of 8 (e.g., Kino et al. 2002), $\Gamma_{\rm f}/\Gamma_{\rm s} \leqslant 1.01$ (Tanihata et al. 2003), and $I_{\rm IS} \sim 1\,R_{\rm s}$ (Koyama et al. 2015). This time we refined the distribution scale of the radio core within 42 μas along its main jet axis, or $4.6 \times 10^3\,R_{\rm s}$ deprojected (see Figure 7). Based on the same assumptions as in Koyama et al. (2015), to explain the further stable distribution scale of the internal shocks, the variation of Lorentz factors of the slower ejecta is constrained to be much smaller, within 30% or $8 \leqslant \Gamma_{\rm s} \leqslant 10$. On the other hand, the radio core wandering of $\Delta D_{\rm IS} \sim 2.6 \times 10^5\,R_{\rm s}$ in Mrk 421 can be explained by the maximum value as $\Gamma_{\rm s} \sim 60$ (with different assumptions; Niinuma et al. 2015). Even by applying the same assumptions to Mrk 421 as those for Mrk 501, the maximum of the slower Lorentz factor is estimated to be $\Gamma_{\rm s} \sim 50$, which is still a few times as large as that of Mrk 501. Therefore, even during the X-ray and VHE γ-ray active states in 2012, the maximum Lorentz factors that explain the stability of Mrk 501's core are roughly a few times smaller than those for Mrk 421's wandering core, based on the internal shock model.

Second, we discuss the possible reasons of no clear association between the astrometric core positions and the high-energy activities for Mrk 501 by comparing the characteristics of the high-energy activity to those of Mrk 421. Both Mrk 501 and Mrk 421 are classified as nearby high-frequency-peaked BL Lacs (HBLs), and their averaged spectra in relatively quiescent states have been similar: usually characterized with a one-zone synchrotron component from radio to X-rays, and its self-Compton component for MeV to VHE γ-ray emission, with the size of the emission region being around 10^{16}–10^{17} cm (e.g., Abdo et al. 2011a, 2011b). However, their typical flaring characteristics are different: the

peak fluxes of Mrk 421 increase significantly in X-rays and/or VHE γ-rays with a slight peak frequency shift, while for Mrk 501 the peak frequency increases by more than a factor of 10 with less variability in the high-energy flux (e.g., Pian et al. 1998; Kataoka et al. 1999; Ahnen et al. 2017). In case of Mrk 421, the flaring spectrum energy densities (SEDs) can usually be explained with one-zone and/or two-zone synchrotron self-Compton (SSC) models (e.g., Aleksić et al. 2015). In the case of Mrk 501 based on Ahnen et al. (2018), at least throughout the whole period of the multiwavelength monitoring between 2012 March and August, the emission in X-rays and VHE γ-rays shows extremely hard spectra, where the X-ray spectral index was less than 2 and the VHE spectral index was around 2 compared to the typical value of $\sim$2.5 (Abdo et al. 2011a; Acciari et al. 2011; Aleksić et al. 2015). Thus, it temporary behaved like an extreme HBL (EHBL), i.e., the synchrotron peak was located above 5 keV, and the inverse-Compton peak was above 0.5 TeV. Two-zone (or more) models were preferred to fit the SEDs, where the one larger zone dominates the averaged spectrum at optical and MeV emission with the size around 10^{16}–10^{17} cm constrained from a minimum variability timescale of $\sim$1 day, and the smaller zone dominates the X-rays and VHE γ-ray flaring emission to have a size of $\sim 10^{15}$ cm, corresponding to a light-crossing time of a few hours (a Doppler factor of 10 was applied). Within the two-zone model, by extrapolating the models fitted to the flaring smaller zone and the averaged larger zone (Figure 7 of Ahnen et al. 2018), the expected fluxes at 43 GHz are estimated to be around less than a few percent and a few tens of percent of the core flux, respectively. In Section 3.1.4 and Figure 6 of Koyama et al. (2016), the possible flux increment of the core peak flux at the third and fourth epochs was discussed ($\sim$30% increment from $\sim$200 mJy at the second epoch within 0.3 mas radius circular beam). This could be associated with the TeV flare; however, since all the other sources at the third and fourth epochs in Table 2 also show higher fluxes than at the other epochs with a similar fraction, the instrumental effects and/or the amplitude calibration errors cannot be rejected. Therefore, not only the flaring smaller zone but also the averaged larger zone may not dominate the 43 GHz core emission, even if they are located close to the radio core. The schematic pictures of the emission zones for this case and the case for Mrk 421 are shown as oranges and red blobs, respectively, in Figure 7. There also could be a possibility that these emission regions that dominate the γ-ray emissions may not be associated with the radio core during this EHBL state, but may be associated with regions farther downstream of the jet, as is suggested for HST-1 in radio galaxy M87 (Cheung et al. 2007) and in narrow-line Seyfert 1 1H 0323+342 (Doi et al. 2018), which are 10^5–10^7 R_s downstream of the central engine.

The other possibility could be the timing of our astrometric observations; they might be too late to follow up the first VHE γ-ray flare in 2011 November (96–180 days after the flare), or too early to follow up the large VHE γ-ray flare in 2012 June (only 3 days after the flare), since the core wander of Mrk 421 was detected around 20–120 days after its historical X-ray flare. Also, even if the core position is wandering, the amount may be too small to be detected with current position accuracy. Whether there is a correlation between the stationarity of radio core positions and the X-ray and/or VHE γ-ray activities needs to be further investigated with denser monitoring of the radio core positions, together with multiwavelength observations during the non-EHBL state since the VHE γ-ray-emitting component in Mrk 501 would be more connected with the radio emission through the one-zone model during the relatively quiescent state (e.g., Abdo et al. 2011a).

The constrained distribution scale of the radio core position is still slightly larger than the spatial resolution of $\sim$30 μas with the Event Horizon Telescope (EHT; Event Horizon Telescope Collaboration et al. 2019), but being comparable to the suggested size of the γ-ray-emitting region of Mrk 501 thanks to its proximity at an order of 10^{16} cm from the SED modeling (e.g., Abdo et al. 2011a). The EHT observations toward the radio core of Mrk 501 will provide a direct hint of whether there exists an emission region with a size comparable to the γ-ray-emitting region in the radio core of the blazar.

5.2. On the Location of the Central Engine

Based on our astrometric results, we further discuss the location of the central engine with respect to the radio core. In Koyama et al. (2016), two possibilities for the location of the central engine in Mrk 501 were discussed: (1) it may be offset from the radio core by $\sim$300 μas northwest, where the axes of the eastern limb and the western limb intersect (the intersection A in Figure 4) based on the internal shock model; and (2) it may be located in the very vicinity of the radio core.

In the case of possibility 1, the core and the NE component are considered to be the internal shocked regions on the western limb and the eastern limb of the double-ridge jet structure (see Figure 4). By assuming the conical jet shape with the apparent opening angle of $\sim$23° (the intrinsic angle of $\sim 1\overset{\circ}{.}6$ by applying $\theta_j = 4°$ from Giroletti et al. 2004), the apex of the two limbs is located $\sim$300 μas northeast of the radio core. This is still within the range of the estimation of the distance between the internal shocks and the central engine based on the internal shock model in Section 5.1, which is estimated to be (2.2–3.7) $\times$ 10^4 R_s deprojected, or 200–300 μas (by taking the maximum estimation of $M_{BH} = 3.4 \times 10^9\, M_\odot$ in Barth et al. 2002). However, the location of the radio core of Mrk 501 is constrained to be fairly stable, concentrated within the thick red cross ($\pm$27 μas; Figure 4), compared to the spatial distribution scale of the NE component (about $\pm$100 μas; Koyama et al. 2016). Thus, the central engine located $\sim$300 μas away from the core is less favorable.

As for possibility 2, the central engine close to the radio core was suggested by Giroletti et al. (2008) with the parsec-scale limb-brightened jet images by the Global Millimeter VLBI Array (GMVA) at 86 GHz, which is similar to the limb-brightened jet of M87 at 43 GHz (Ly et al. 2007). Based on the core shift measurement of Mrk 501 at lower frequencies (Croke et al. 2010), the location of the convergence point of the core shift is estimated to be located in the very vicinity of the 43 GHz radio core, 30^{+45}_{-23} μas upstream of it, which corresponds to about a 1σ position error of this VLBA astrometry. The distance between the central engine and the radio core is also within the range of the internal shock model. In this case, the apparent jet opening angle is $\sim$118° derived from the position angle difference of the NE component and the southern jet, and the intrinsic jet opening angle is $\sim$13°. The intrinsic half jet opening angle is $\sim 6\overset{\circ}{.}5$, which is larger than the assumed jet viewing angle of 4°. This may imply that we are observing the so-called "down-the-pipe" region (Clausen-Brown et al. 2013); however, more detailed inner jet structure should be investigated with higher-resolution

images. The true location of the central engine will be further investigated by analyzing multifrequency astrometric core shift measurements and the jet width along the jet axis, as is performed for nearby radio galaxies (e.g., Hada et al. 2013, 2018; Tseng et al. 2016; Giovannini et al. 2018; Nakahara et al. 2018; Nakamura et al. 2018).

6. Conclusion

In order to investigate the precise radio core position in blazars and to search for any relation with high-energy activity, we have conducted multiepoch high-precision astrometric observations of the blazar Mrk 501 with the VLBA at 43 GHz for the first time during its X-ray and VHE γ-ray active state. Below, we summarize the main conclusions in this work.

1. We achieve an accuracy of $\sim$50 μas for the radio core position of Mrk 501 relative to that of 3C 345, and $\sim$70 μas for that relative to NRAO 512 for each epoch. By resolving the jet structure, the radio core position of Mrk 501 over six epochs in 1 yr during 2012–2013 February remained stable within 42 μas along the SE jet direction relative to 3C 345 and within 53 μas along the NE jet relative to NRAO 512, with $\pm1\sigma$ error (68% confidence level) of the weighted-mean position, by assuming that the radio core positions are stationary in the orthogonal direction of their jets. By combining our results with the VERA astrometry in 2011, the radio core position of Mrk 501 still remained stable using the same sources. The VLBA astrometry by using the faint point-source-like calibrator 1659+399 also showed that there is no significant core peak position change in Mrk 501.
2. We pinpointed the relative radio core position of Mrk 501 around four times as accurate as that with the previous VERA astrometry at 43 GHz. Although Mrk 501 was flaring in VHE γ-rays just before the fourth epoch and active also in X-rays and VHE at least during the first four epochs of the VLBA observations, the radio core remained stable. This result is in contrast to another case of the famous nearby TeV blazar Mrk 421, which showed a clear radio core position change soon after the large X-ray flare in 2011 (Niinuma et al. 2015). The location of the radio core of Mrk 501 was limited within the deprojected scale of $4.6 \times 10^3\,R_{\rm s}$ or 0.5 pc, which is about 1/30 that of Mrk 421. The tightly constrained radio core position can be explained with the standard internal shock model with smaller variation of Lorentz factors of ejecta than the case for our VERA astrometry (Koyama et al. 2015) and a few times as small as those for explaining Mrk 421's wandering core (Niinuma et al. 2015). The different results of the radio core astrometry during the active states for the two nearby blazars can also be understood as the different characteristics of the high-energy activities. Especially, the extremely hard spectrum (i.e., EHBL-like state) for Mrk 501 at X-rays and VHE γ-rays temporarily during our observations suggests that the 43 GHz radio core emission may not be dominated by the high-energy emitting region. Denser monitoring of the radio core position during the non-EHBL state but relatively quiescent state may enable us to study any connection between the γ-ray emission and radio emission.
3. Two cases of the location of the central engine were discussed: the central engine located $\sim$300 μas northeast of the core on the western limb of the jet, and that located in the very vicinity of the core. For the distant case, the internal shock model has difficulty explaining both the radio core and the NE component on the eastern and western limb, respectively, with the similar Lorentz factors, since the radio core is fairly stable. The true location of the central engine will be further investigated by combining the detailed jet width analysis with respect to the distance from the central engine.

We thank the anonymous referee for careful reading and offering constructive comments for improving the paper. S.K. thanks Masanori Nakamura and Keiichi Asada for helpful comments and encouragement. This paper is based on observations carried out with the VLBA. The National Radio Astronomy Observatory is a facility of the National Science Foundation operated under cooperative agreement by Associated Universities, Inc. This work made use of the Swinburne University of Technology software correlator (Deller et al. 2011), developed as part of the Australian Major National Research Facilities Programme and operated under license. This work was done with the contribution of the Italian Ministry of Foreign Affairs and University and Research for the collaboration project between Italy and Japan. This work is partially supported by JSPS KAKENHI grant Nos. 18K03656 (M.K.), 18H03721 (K.N., M.K., K.H.), 24340042 (A.D.), and 25120007 (M.H., K.H., K.A.). K.A. is a Jansky Fellow of the National Radio Astronomy Observatory. The Black Hole Initiative at Harvard University is financially supported by a grant from the John Templeton Foundation. K.A. is financially supported in part by a grant from the National Science Foundation (AST-1614868). G.Y.Z is supported by the Korea Research Fellowship Program through the National Research Foundation of Korea (NRF) funded by the Ministry of Science and ICT (NRF-2015H1D3A1066561).

Facility: VLBA.

Appendix A
Astrometry

A.1. Observation Equations

We consider an observing schedule of a simple phase-referencing with a pair consisting of a target (T) and a calibrator (C1), both of which provide signal-to-noise ratios high enough to do self-calibration. After determination of amplitude-gain, delay, and delay-rate solutions, all we have to consider is phase terms. Observed visibility phases, $\phi_{\rm OBS}$, involve various phase terms:

$$\phi^{\rm C1}_{\rm OBS} = \phi^{\rm C1}_{\rm stru} + \phi^{\rm C1}_{\rm pos} + \phi^{\rm C1}_{\rm inst} + \phi^{\rm C1}_{\rm geo} + \phi^{\rm C1}_{\rm atmo} + \phi^{\rm C1}_{\rm rapid}, \quad (1)$$

$$\phi^{\rm T}_{\rm OBS} = \phi^{\rm T}_{\rm stru} + \phi^{\rm T}_{\rm pos} + \phi^{\rm T}_{\rm inst} + \phi^{\rm T}_{\rm geo} + \phi^{\rm T}_{\rm atmo} + \phi^{\rm T}_{\rm rapid}, \quad (2)$$

where $\phi^{\rm C1}$ and $\phi^{\rm T}$ are phase terms for C1 and T, respectively. $\phi_{\rm stru}$ is a phase term originating in source structure; $\phi_{\rm pos}$ is a positional-phase delay relative to a phase-tracking center; $\phi_{\rm inst}$ is an instrumental phase delay; $\phi_{\rm geo}$ is a geometric-phase delay error; $\phi_{\rm atmo}$ is a tropospheric/ionospheric-phase delay error; $\phi_{\rm rapid}$ is a rapidly variable phase due to the nonuniform component of water vapor flowing at low altitude (<10 km). We ignore thermal phase noise and calibration errors in the

equations. We deal with the phase terms of source position and structure separately because we will show an astrometric term and its error expressly at the final stage. Timescales of the change of these phase error components are usually more than several tens of minutes, except for $\phi_{\rm rapid}$, in which the timescale is typically a few minutes or less (Ulvestad et al. 1998).

A.2. Calibration Process

We assume that sufficiently feasible source structure models for C1 and T in the form of a series of clean components (CC models) are obtained:

$$\Phi^{\rm C1}_{\rm CC} = \Phi^{\rm C1}_{\rm stru} + \Phi^{\rm C1}_{\rm CCpos}, \tag{3}$$

$$\Phi^{\rm T}_{\rm CC} = \Phi^{\rm T}_{\rm stru} + \Phi^{\rm T}_{\rm CCpos}, \tag{4}$$

where $\Phi_{\rm stru}$ is the phase component of source structure and $\Phi_{\rm CCpos}$ is a possible positional-phase delay error (relative to a phase-tracking center) that may be included in the CC model during iterative clean and self-calibration procedures.

Before phase-referencing using C1, we desire to separate only the structure phase from the raw visibility of C1. Practically, however, we can only separate the visibility phase equivalent to the CC model from the other phase components by performing fringe fitting on C1 using its CC model:

$$\phi^{\rm C1}_{\rm OBS} = \Phi^{\rm C1}_{\rm CC} + \Phi^{\rm C1}_{\rm SN1}, \tag{5}$$

where

$$\Phi^{\rm C1}_{\rm SN1} = -\Phi^{\rm C1}_{\rm CCpos} + \phi^{\rm C1}_{\rm pos} + \phi^{\rm C1}_{\rm inst} + \phi^{\rm C1}_{\rm geo} + \phi^{\rm C1}_{\rm atmo} + \phi^{\rm C1}_{\rm rapid}. \tag{6}$$

$\Phi^{\rm C1}_{\rm SN1}$ is an antenna-based solution table obtained through the fringe fitting (or the self-calibration). For the purpose of subtracting only the structure phase ($\Phi^{\rm C1}_{\rm stru}$), the positional-phase delay error in the CC model ($\Phi^{\rm C1}_{\rm CCpos}$) would remain.

With the solution table $\Phi^{\rm C1}_{\rm SN1}$, we correct the target data so that its phase is free from rapid phase fluctuations due to water vapor as follows:

$$\begin{aligned}
\phi^{\rm T}_{\rm PR} &= \phi^{\rm T}_{\rm OBS} - \Phi^{\rm C1}_{\rm SN1} \\
&= \phi^{\rm T}_{\rm stru} + \phi^{\rm T}_{\rm pos} + \phi^{\rm T}_{\rm inst} + \phi^{\rm T}_{\rm geo} + \phi^{\rm T}_{\rm atmo} + \phi^{\rm T}_{\rm rapid} \\
&\quad - (-\Phi^{\rm C1}_{\rm CCpos} + \phi^{\rm C1}_{\rm pos} + \phi^{\rm C1}_{\rm inst} + \phi^{\rm C1}_{\rm geo} + \phi^{\rm C1}_{\rm atmo} + \phi^{\rm C1}_{\rm rapid}) \\
&= \phi^{\rm T}_{\rm stru} + \Phi^{\rm C1}_{\rm CCpos} + \Delta\phi^{\rm T-C1}_{\rm pos} + \Delta\phi^{\rm T-C1}_{\rm inst} \\
&\quad + \Delta\phi^{\rm T-C1}_{\rm geo} + \Delta\phi^{\rm T-C1}_{\rm atmo} + \Delta\phi^{\rm T-C1}_{\rm rapid} \\
&\approx \phi^{\rm T}_{\rm stru} + \Phi^{\rm C1}_{\rm CCpos} + \Delta\phi^{\rm T-C1}_{\rm pos} + \Delta\phi^{\rm T-C1}_{\rm geo} + \Delta\phi^{\rm T-C1}_{\rm atmo},
\end{aligned} \tag{7}$$

where $\Delta\phi^{\rm T-C1}_i \equiv \phi^{\rm T}_i - \phi^{\rm C1}_i$ represents a differential phase term. We consider $\Delta\phi^{\rm C2-C1}_{\rm rapid} \approx 0$ because its random fluctuation is not responsible for a systematic residual and, therefore, must be averaged out. Furthermore, $\Delta\phi^{\rm C2-C1}_{\rm inst} \approx 0$ because an identical receiving system is used. This is a normal phase referencing, which has been commonly used (Beasley & Conway 1995). The other differential phase terms may not be zero, and they cause long-term phase drifts. As we mentioned above, the timescales are usually more than several tens of minutes. These remaining phase errors may cause some apparent position shift and the degradation of image dynamic range.

The resultant phase-referenced image exhibits the structure of the target with some position shift and distortion. Conventionally, the astrometric position had been measured with a Gaussian model fitting to the whole structure or a conceivable target component. Actually, however, the radio source frequently includes a significant structure deviated from a Gaussian profile, for example, the core–jet structure of AGNs and the cluster of astronomical masers. It is worthwhile to subtract the structure phase ($\phi^{\rm T}_{\rm stru}$) before the position measurement. Practically, we can subtract the visibility phase equivalent to the CC model ($\phi^{\rm T}_{\rm CC}$) from the phase-referenced visibility through the self-calibration:

$$\phi^{\rm T}_{\rm PR} = \phi^{\rm T}_{\rm CC} + \Phi_{\rm SN2}\ , \tag{8}$$

where

$$\Phi_{\rm SN2} = -\Delta\Phi^{\rm T-C1}_{\rm CCpos} + \Delta\phi^{\rm T-C1}_{\rm pos} + \Delta\phi^{\rm T-C1}_{\rm geo} + \Delta\phi^{\rm T-C1}_{\rm atmo}. \tag{9}$$

Consequently, we obtain the target image as a point source with a positional shift equivalent to astrometric information and the distortion due to remaining errors that are uncorrectable. The position measurement with a Gaussian model fitting results in the astrometric position $\Delta\phi^{\rm T-C1}_{\rm pos}$ with an error of $-\Delta\Phi^{\rm T-C1}_{\rm CCpos} + \Delta\phi^{\rm T-C1}_{\rm geo} + \Delta\phi^{\rm T-C1}_{\rm atmo}$. The error component $\Delta\Phi^{\rm T-C1}_{\rm CCpos}$ can be determined by image analyses for the self-calibrated images of T and C1.

Appendix B
Estimation of Position Errors

The position errors were estimated basically by following the Appendix of Koyama et al. (2015). Our VLBA observations can reduce two of seven error budgets because of the following advantages: (i) ionospheric effects are close to zero because the observing frequency is 43 GHz, and (ii) the instrumental phase error is zero because we observe both the target and the calibrator with the same VLBA system.

We summarize the estimated error budget in our phase-referencing observations in Table 4. Since these sources of errors contribute independently of each other, the total errors at each epoch can be obtained as the root sum square of them. Figure 8 shows the phase-referenced images of all the targets after performing the new data reduction procedure. Thanks to the new reduction procedure, the higher signal-to-noise ratios in the images compared to those with the standard reduction procedure improved the random errors by a few times, but it did not improve the total errors since tropospheric errors are the most dominant (only within a few microarcseconds of improvement). As for the estimation of tropospheric zenith delay error, by adopting a typical $\sim$3 cm misestimation of the zenith delay for the VLBA (e.g., Reid et al. 1999), this introduces the shift of the absolute position up to $\sim$37 μas at 43 GHz for the local source zenith angle $Z \sim 50^\circ$ and the source separation $\Delta Z = 1.^\circ5$, for example. The ionospheric error is estimated to be <1 μas at 43 GHz (Mannucci et al. 1998). The core identification error is defined in Section 3.

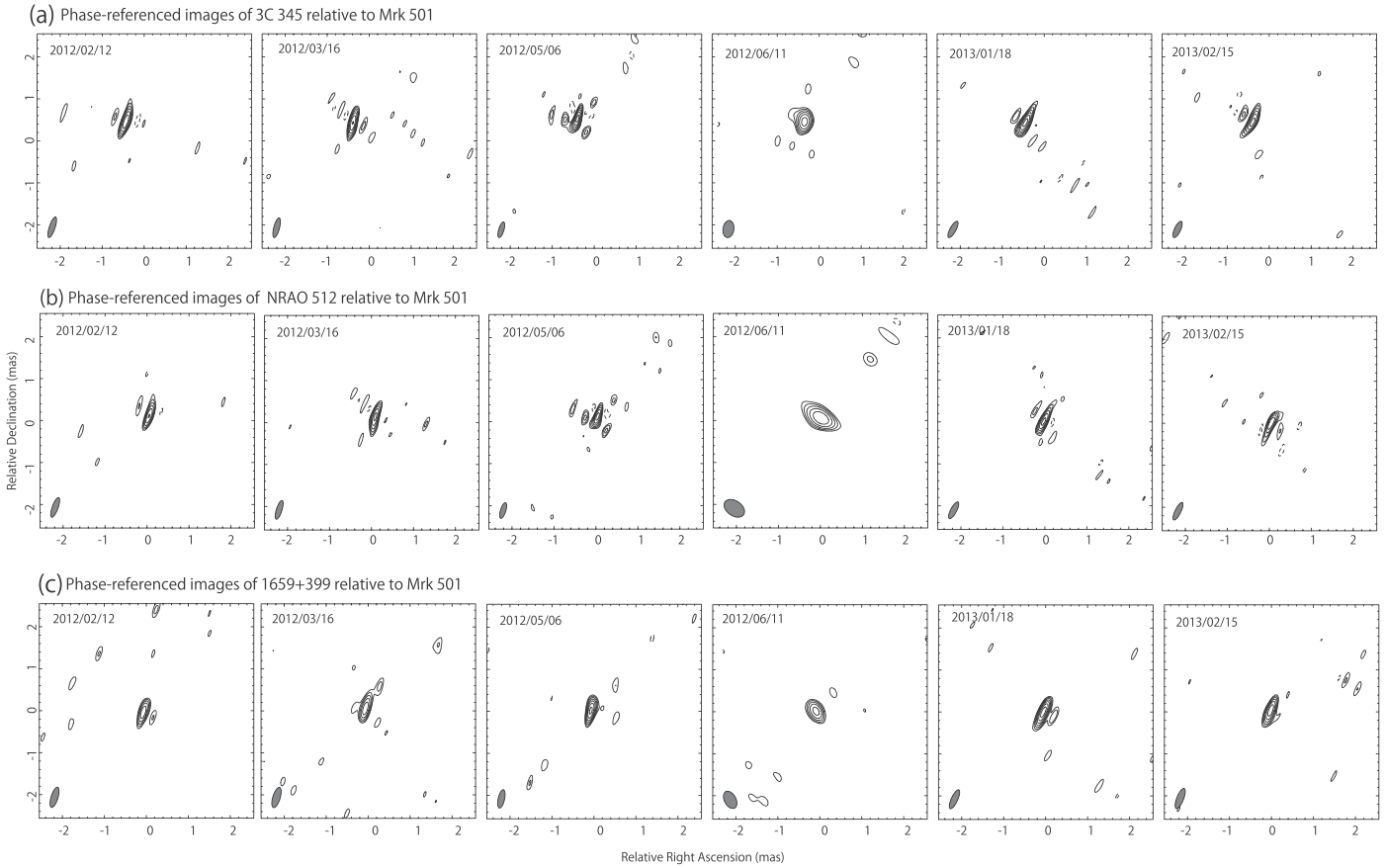

Figure 8. Phase-referenced images of 3C 345, NRAO 512, and 1659+399 referencing to Mrk 501's core, after removing the source structures of both calibrators and targets (see the data reduction in Section 3 and Appendix A). The gray ellipse at the lower left of each image shows the synthesized beam size (FWHM). The rms noise in the images is summarized in Table 3. Contours start at the $\pm 3\sigma$ level, increasing by factors of $\sqrt{2}$.

Table 4
Estimated Positional Error Budgets of Mrk 501 in the Phase-referencing Observation

Phase-referenced Pair	Epoch	$\sigma_{\rm random}$		$\sigma_{\rm trop}$	$\sigma_{\rm ion}$	$\sigma_{\rm Earth}$		$\sigma_{\rm ant}$		$\sigma_{\rm coord}$		$\sigma_{\rm id}$		$\sigma_{\rm rss}$	
		x	y			x	y	x	y	x	y	x	y	x	y
(1)	(2)	(3)	(4)	(5)	(6)	(7)	(8)	(9)	(10)	(11)	(12)	(13)	(14)	(15)	(16)
Mrk 501−3C 345	2012 Feb 12	3	8	49	<1	1	5	2	3	3	5	15	15	51	52
	2012 Mar 16	3	8	49	<1	1	5	2	3	3	5	8	10	50	51
	2012 May 6	2	5	49	<1	1	5	2	3	3	5	6	6	49	50
	2012 Jun 11	7	10	49	<1	1	5	2	3	3	5	9	6	50	51
	2013 Jan 18	3	5	49	<1	1	5	2	3	3	5	18	10	52	51
	2013 Feb 15	4	7	49	< 1	1	5	2	3	3	5	10	5	50	50
Mrk 501−NRAO 512	2012 Feb 12	4	10	60	<1	1	5	2	3	3	5	27	43	66	75
	2012 Mar 16	4	9	60	<1	1	5	2	3	3	5	33	56	69	83
	2012 May 6	3	7	60	<1	1	5	2	3	3	5	8	19	61	64
	2012 Jun 11	14	12	60	<1	1	5	2	3	3	5	6	17	62	64
	2013 Jan 18	4	7	60	<1	1	5	2	3	3	5	23	22	65	65
	2013 Feb 15	5	8	60	<1	1	5	2	3	3	5	10	13	61	63
Mrk 501−1659+399	2012 Feb 12	6	12	37	<1	1	5	2	3	3	5	7	16	39	43
	2012 Mar 16	6	13	37	<1	1	5	2	3	3	5	9	11	39	42
	2012 May 6	3	7	37	<1	1	5	2	3	3	5	6	6	38	39
	2012 Jun 11	11	14	37	<1	1	5	2	3	3	5	4	7	39	41
	2013 Jan 18	3	5	37	<1	1	5	2	3	3	5	18	10	42	40
	2013 Feb 15	4	8	37	<1	1	5	2	3	3	5	9	5	39	39

Note. The units are in μas. Columns are as follows: (1) phase-referencing pair; (2) observing epoch; (3, 4) random error estimated by beamwidth over 2 times signal-to-noise ratio in the direction of R.A. and decl.; (5) tropospheric residual errors; (6) ionospheric residual errors; (7, 8) Earth orientation parameter error in R.A. and decl.; (9, 10) antenna position error in R.A. and decl.; (11, 12) a priori source coordinates error in R.A. and decl.; (13, 14) core identification error in R.A. and decl. The units are in μas. The error contributions from the geometrical errors (7)–(12) are estimated based on the simulation presented in Pradel et al. (2006). Total error in R.A. (15) and in decl. (16) is estimated as the root sum square of each error.

Appendix C
Core Peak Positions of Mrk 501 Relative to 1659+399

The source 1659+399 was used for the consistency check for the astrometry with 2- to 4-minute scans per epoch. Table 5 and Figure 9 shows the measured core positions of Mrk 501 and those along its jet axis relative to the peak position of 1659 +399 for all the observations. Typically, the core position error of 1659+399 relative to Mrk 501 is estimated to be ∼39 μas in R.A. and ∼42 μas in decl. The tropospheric zenith delay errors correspond to the position error of ∼37 μas for the separation of 1°.46 between Mrk 501 and 1659+399. The signal-to-noise ratios of the phase-referenced images range from 14 to 26.

We performed a *t*-test of the phase-referenced core positions over the six epochs, for the consistency check of the results relative to 3C 345. We found that the core positions of Mrk 501 relative to 1659+399 coincide along the position angle of the SE jet of Mrk 501 with the significance probability of 71%. This probability is comparable to that of the results with 3C 345. The weighted-mean position and error along the SE jet is 28 ± 17 μas. Thus, we can conclude that the phase-referenced core peak positions of Mrk 501 relative to 1659 +399 lie within 33 μas (±1σ) along the jet direction, and we confirmed that the distribution range is consistent with the measurements relative to 3C 345.

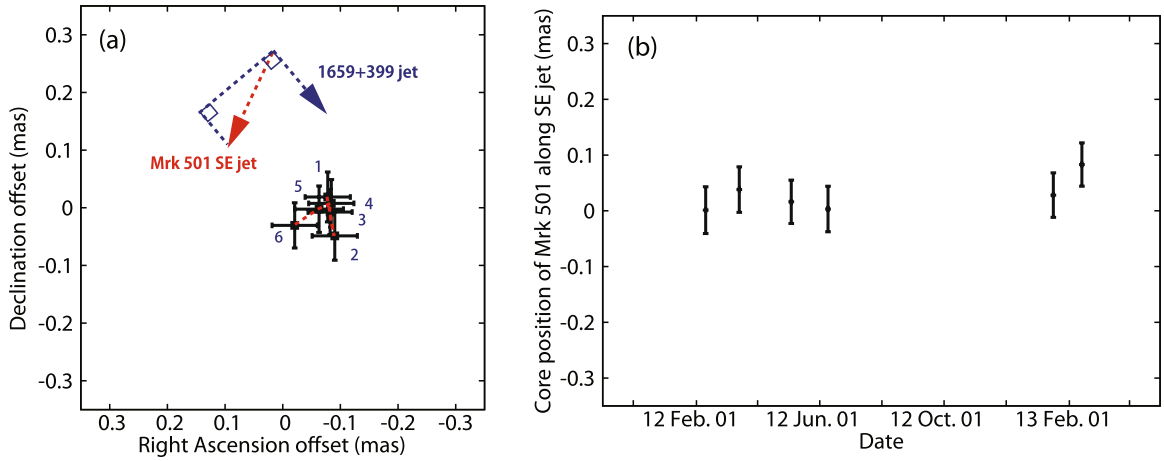

Figure 9. Measured radio core position of Mrk 501 relative to the radio core of calibrator 1659+399. (a) The blue arrow indicates the jet direction of 1659+399, and the red arrow indicates the direction of Mrk 501's SE jet. (b) The horizontal and vertical axes show the time and the positional offsets along the direction of Mrk 501's SE jet with respect to the position of the first epoch. The positional offsets are extracted along the perpendicular direction to the jet of 1659+399 and recalculated along the direction of Mrk 501's SE jet.

Table 5
Image Qualities and Core Positions of Phase-referenced Images of Mrk 501

Phase-referenced Pair	Epoch	I_p (mJy beam^{-1})	σ_{rms} (mJy beam^{-1})	I_p/σ_{rms}	$\Delta\alpha$ (mas)	$\Delta\delta$ (mas)
(1)	(2)	(3)	(4)	(5)	(6)	(7)
Mrk 501−1659+399	2012 Feb 12	116	7.41	16	−0.078 ± 0.039	0.019 ± 0.043
	2012 Mar 16	95.4	6.20	15	−0.090 ± 0.039	−0.048 ± 0.042
	2012 May 6	180	6.81	26	−0.082 ± 0.038	−0.007 ± 0.039
	2012 Jun 11	154	11.0	14	−0.084 ± 0.039	0.008 ± 0.041
	2013 Jan 18	111	3.77	29	−0.063 ± 0.042	−0.002 ± 0.040
	2013 Feb 15	219	10.3	21	−0.021 ± 0.039	−0.030 ± 0.039

Note. Same as Table 3.

ORCID iDs

Shoko Koyama https://orcid.org/0000-0002-3723-3372
Motoki Kino https://orcid.org/0000-0002-2709-7338
Akihiro Doi https://orcid.org/0000-0003-4384-9568
Kotaro Niinuma https://orcid.org/0000-0002-8169-3579
Marcello Giroletti https://orcid.org/0000-0002-8657-8852
Kazunori Akiyama https://orcid.org/0000-0002-9475-4254
Gabriele Giovannini https://orcid.org/0000-0003-4916-6362
Guang-Yao Zhao https://orcid.org/0000-0002-4417-1659
Eduardo Ros https://orcid.org/0000-0001-9503-4892
Jun Kataoka https://orcid.org/0000-0003-2819-6415
Monica Orienti https://orcid.org/0000-0003-4470-7094
Kazuhiro Hada https://orcid.org/0000-0001-6906-772X
Hiroshi Nagai https://orcid.org/0000-0003-0292-3645
Hideyuki Kobayashi https://orcid.org/0000-0001-8066-1631
Mareki Honma https://orcid.org/0000-0003-4058-9000
Rocco Lico https://orcid.org/0000-0001-7361-2460

References

Abdo, A. A., Ackermann, M., Ajello, M., et al. 2011a, ApJ, 727, 129
Abdo, A. A., Ackermann, M., Ajello, M., et al. 2011b, ApJ, 736, 131
Acciari, V. A., Arlen, T., Aune, T., et al. 2011, ApJ, 729, 2
Agudo, I. 2009, in ASP Conf. Ser. 402, Approaching Micro-Arcsecond Resolution with VSOP-2: Astrophysics and Technologies, ed. Y. Hagiwara et al. (San Francisco, CA: ASP), 330
Aharonian, F. A., Akhperjanian, A. G., Barrio, J. A., et al. 1999, A&A, 342, 69
Ahnen, M. L., Ansoldi, S., Antonelli, L. A., et al. 2017, A&A, 603, A31
Ahnen, M. L., Ansoldi, S., Antonelli, L. A., et al. 2018, A&A, 620, A181
Aleksić, J., Ansoldi, S., Antonelli, L. A., et al. 2015, A&A, 578, A22
Bartel, N., Herring, T. A., Ratner, M. I., Shapiro, I. I., & Corey, B. E. 1986, Natur, 319, 733
Barth, A. J., Ho, L. C., & Sargent, W. L. W. 2002, ApJL, 566, L13
Bartoli, B., Bernardini, P., Bi, X. J., et al. 2012, ApJ, 758, 2
Beasley, A. J., & Conway, J. E. 1995, in ASP Conf. Ser. 82, Very Long Baseline Interferometry and the VLBA, ed. J. A. Zensus, P. J. Diamond, & P. J. Napier (San Francisco, CA: ASP), 327
Blasi, M. G., Lico, R., Giroletti, M., et al. 2013, A&A, 559, A75
Catanese, M., Bradbury, S. M., Breslin, A. C., et al. 1997, ApJL, 487, L143
Cheung, C. C., Harris, D. E., & Stawarz, Ł. 2007, ApJL, 663, L65
Clausen-Brown, E., Savolainen, T., Pushkarev, A. B., Kovalev, Y. Y., & Zensus, J. A. 2013, A&A, 558, A144
Croke, S. M., O'Sullivan, S. P., & Gabuzda, D. C. 2010, MNRAS, 402 259
Deller, A. T., Brisken, W. F., Phillips, C. J., et al. 2011, PASP, 123, 275
Doi, A., Hada, K., Kino, M., Wajima, K., & Nakahara, S. 2018, ApJL, 857, L6
Event Horizon Telescope Collaboration, Akiyama, K., Alberdi, A., et al. 2019, ApJL, 875, L1
Fey, A. L., Gordon, D., & Jacobs, C. S. (ed.) 2009, IERS Technical Note 35, The Second Realization of the International Celestial Reference Frame by Very Long Baseline Interferometry (Frankfurt: Bundesamts für Kartographie und Geodäsie)
Ghisellini, G., Tavecchio, F., & Chiaberge, M. 2005, A&A, 432, 401
Giovannini, G., Savolainen, T., Orienti, M., et al. 2018, NatAs, 2, 472
Giroletti, M., Giovannini, G., Cotton, W. D., et al. 2008, A&A, 488, 905
Giroletti, M., Giovannini, G., Feretti, L., et al. 2004, ApJ, 600, 127
Guetta, D., Ghisellini, G., Lazzati, D., & Celotti, A. 2004, A&A, 421, 877
Hada, K., Doi, A., Kino, M., et al. 2011, Natur, 477, 185
Hada, K., Doi, A., Wajima, K., et al. 2018, ApJ, 860, 141
Hada, K., Giroletti, M., Kino, M., et al. 2014, ApJ, 788, 165
Hada, K., Kino, M., Doi, A., et al. 2013, ApJ, 775, 70
Jorstad, S. G., Marscher, A. P., Morozova, D. A., et al. 2017, ApJ, 846, 98
Kapanadze, B., Dorner, D., Romano, P., et al. 2017, MNRAS, 469, 1655
Kataoka, J., Mattox, J. R., Quinn, J., et al. 1999, ApJ, 514, 138
Kino, M., Mizuta, A., & Yamada, S. 2004, ApJ, 611, 1021
Kino, M., Takahara, F., & Kusunose, M. 2002, ApJ, 564, 97
Koyama, S., Kino, M., Doi, A., et al. 2015, PASJ, 67, 67
Koyama, S., Kino, M., Giroletti, M., et al. 2016, A&A, 586, A113
Lico, R., Giroletti, M., Orienti, M., et al. 2012, A&A, 545, A117
Ly, C., Walker, R. C., & Junor, W. 2007, ApJ, 660, 200
Mannucci, A. J., Wilson, B. D., Yuan, D. N., et al. 1998, RaSc, 33, 565
Marscher, A. P., Jorstad, S. G., D'Arcangelo, F. D., et al. 2008, Natur, 452 966
Nakahara, S., Doi, A., Murata, Y., et al. 2018, ApJ, 854, 148
Nakamura, M., Asada, K., Hada, K., et al. 2018, ApJ, 868, 146
Niinuma, K., Kino, M., Doi, A., et al. 2015, ApJL, 807, L14
Pian, E., Vacanti, G., Tagliaferri, G., et al. 1998, ApJL, 492, L17
Pradel, N., Charlot, P., & Lestrade, J.-F. 2006, A&A, 452, 1099
Reid, M. J., Readhead, A. C. S., Vermeulen, R. C., & Treuhaft, R. N. 1999, ApJ, 524, 816
Schinzel, F. K., Lobanov, A. P., Taylor, G. B., et al. 2012, A&A, 537, A70
Sokolovsky, K. V., Kovalev, Y. Y., Lobanov, A. P., et al. 2010, arXiv:1001.2591
Sootome, T., Sugizaki, M., Mihara, T., et al. 2011, ATel, 3752, 1
Spada, M., Lazzati, D., Ghisellini, G., & Celotti, A. 2001, MmSAI, 72, 157
Tanihata, C., Takahashi, T., Kataoka, J., & Madejski, G. M. 2003, ApJ, 584, 153
Tseng, C.-Y., Asada, K., Nakamura, M., et al. 2016, ApJ, 833, 288
Ulvestad, J. S., Roy, A. L., Colbert, E. J. M., & Wilson, A. S. 1998, ApJ, 496, 196
Wagner, R. M. 2008, MNRAS, 385, 119